Required Current Control Bandwidth and Allowable Voltage-Detection Delay for DSP-Based Current-Source-Type Electric Motor Emulator

Gensui Tanaka[1], Hiroki Watanabe[2], Jun-ichi Itoh[2*]
1 Department of Science of Technology Innovation, Nagaoka University of Technology, Nagaoka, Japan
2 Department of Electrical, Electronics, and Information Engineering, Nagaoka University of Technology, Nagaoka, Japan
*itoh@vos.nagaokaut.ac.jp

***Abstract*—This paper analyzes the allowable voltage-detection delay and the required current-control bandwidth for a digital signal processor (DSP)-based current-source-type electric motor emulator (EME). The interaction between the current control loops of the inverter under test (IUT) and the EME is investigated to clarify the stability condition of the emulator system. The required EME current-control bandwidth is analyzed under practical conditions where PWM output delay and current-sensing delay are approximated as first-order lag systems. The analytical results indicate that the required EME current-control bandwidth is approximately 4.8 times that of the IUT, whose current-control bandwidth is 500 Hz. In addition, the allowable voltage-detection delay when a low-pass filter (LPF) is used is investigated, and phase-lead compensation is applied to mitigate the delay. Experimental results verify the validity of the analysis and demonstrate stable motor emulation under the derived design conditions.**

Keywords—Motor emulator, Digital signal processor (DSP), Current control,

I. INTRODUCTION (*HEADING 1*)

Electric motor drive systems with high-power ratings are widely used in industrial applications such as traction systems, renewable energy systems, and large-scale manufacturing equipment. The development and testing of such high-power motor drive systems are challenging because they require large-capacity motor test benches, which increase costs, installation space, and safety requirements. In addition, testing under various operating conditions is difficult because the motor parameters and mechanical load cannot be easily modified. To address these issues, electric motor emulators (EMEs) have been proposed as an alternative test platform that reproduces motor behavior using power electronic converters and motor models [1]–[6]. The primary advantage of an EME is that it enables testing of an inverter under test (IUT) and evaluation of the emulated motor behavior without a large motor test bench. In addition, motor parameters and test conditions, such as rotational speed and load, can be flexibly adjusted. Consequently, EMEs reduce development costs and improve testing flexibility in motor drive development.

EMEs are classified into two types: voltage-source-type and current-source-type. The current-source-type EME reproduces the motor current, including transient characteristics. This type is applicable regardless of the IUT control method because it is based on current control. Consequently, the current-source-type EME is suitable for inverter test systems. The major difference between a current-source-type EME and an actual motor test bench is that the IUT output voltage must be detected and used to generate the current command. The transient response accuracy of the current-source-type EME depends on the delay in voltage detection because the motor current command is calculated from the detected IUT output voltage based on the motor model [7]–[10]. One challenge in achieving low detection delay is that the IUT output voltage has a pulse-width-modulated (PWM) waveform. Moreover, interference between the current control loops of the IUT and the current-source-type EME occurs when the IUT employs current control because both controllers regulate the same current within their respective closed-loop bandwidths [11]–[12]. Thus, reducing the voltage detection delay and increasing the current control bandwidth are important for achieving accurate motor emulation.

However, achieving a high dynamic response in high-power converters is relatively difficult. When an EME is used to test high-power motor drive systems, the power converter in the emulator must also have a high power rating. In such systems, the achievable current-control bandwidth is often limited by the switching frequency and controller performance. Consequently, designing an EME that satisfies the high-current control bandwidth becomes challenging. As described above, interference between the current control loops of the IUT and the EME may cause system instability. The bandwidth must be determined through trial-and-error design if the minimum current-control bandwidth required for the EME to avoid this interference is not specified. This approach increases development time and makes the practical implementation of EMEs difficult, especially for high-power applications. In addition, accurate detection of the IUT output voltage is required to calculate the motor current command in the EME. Conventional approaches often employ high-speed voltage-detection circuits or high-performance controllers to minimize detection delay. However, such approaches increase system cost and complexity, which is undesirable for practical inverter testing environments. Therefore, it is important to clarify the minimum current-control bandwidth required for stable motor emulation and to develop a practical voltage-detection method that does not rely on high-performance hardware.

This paper first derives the minimum current-control bandwidth required for the EME to prevent interference between the current-control loops of the IUT and the EME. In

This work was supported by JST SPRING, Japan Grant Number JPMJSP2189.

addition, this paper uses voltage detection with a low-pass filter (LPF) to enable low-cost implementation and implements the EME entirely on a digital signal processor (DSP). The contributions of this paper are twofold. First, this paper focuses on clarifying the minimum current-control bandwidth required for an EME to prevent interference between the current-control loops of the IUT and the EME. This analysis is particularly important when considering applications to large-capacity motor drive systems, where achieving a high current-control bandwidth is inherently difficult. Second, this paper investigates a voltage detection method based on an LPF, which is easy to implement but introduces a relatively large detection delay. Conventional approaches often rely on high-performance voltage-detection hardware to reduce detection latency. In contrast, this paper clarifies the allowable delay in voltage detection and demonstrates that stable motor emulation can be achieved without relying on high-performance voltage-detection hardware. These results provide a practical design guideline for implementing a current-source-type EME, enabling stable motor emulation without high-performance voltage-detection hardware, while considering applications to large-capacity motor-drive systems.

II. Current-Source-Type Electric Motor Emulator

A. Hardware configuration

Fig. 1 shows the configuration of the inverter test system using a current-source-type EME. The current-source-type EME connects only the three-phase power lines and the position or speed sensor lines to the IUT and its controller. This configuration is the same as a motor test bench, thereby preserving its advantages. In addition, this study uses an inductor and a two-level three-phase inverter as the coupling and power-conversion circuit. There are alternative options for couplings and power-conversion circuits, but this configuration is the simplest.

B. Controller configuration

Fig. 2 shows the block diagram of the inverter test system using the current-source-type EME. The controller detects the phase voltages and currents of the IUT. The motor model calculates the motor current from the detected phase voltage, which is transformed into the dq-axis. The motor model is a voltage-input, current-output model for the current-source-type EME. This paper adopts the state equation as the simplest

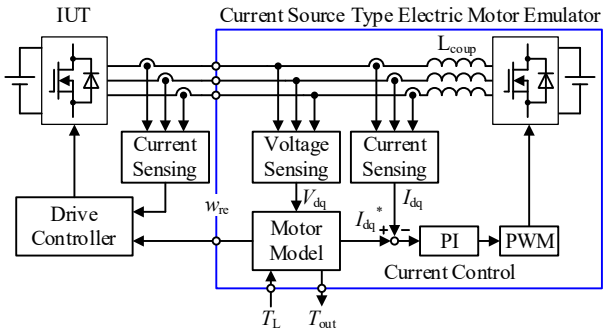

Fig. 1 Configuration of the inverter test system using a current-source-type EME. The EME is connected to the inverter under test (IUT) through three-phase power lines and sensor signals. This configuration emulates the motor behavior while maintaining the same interface as a conventional motor test bench.

motor model in order to focus on the current response. Note that electromagnetic field (EMF) analysis results that consider magnetic characteristics and other factors can also be used when more detailed motor characteristics need to be evaluated. The state equation of an interior permanent magnet synchronous motor (IPMSM) based on the dq-axis is expressed as

$$P\begin{bmatrix} i_d \\ i_q \end{bmatrix} = \begin{bmatrix} -\frac{R_a}{L_d} & \omega_{re}\frac{L_q}{L_d} \\ -\omega_{re}\frac{L_q}{L_d} & -\frac{R_a}{L_q} \end{bmatrix}\begin{bmatrix} i_d \\ i_q \end{bmatrix} + \begin{bmatrix} \frac{v_d}{L_d} \\ \frac{v_q}{L_q} \end{bmatrix} + \begin{bmatrix} 0 \\ -\frac{\omega_{re}\psi_m}{L_q} \end{bmatrix}, \quad \text{.....(1)}$$

where i_d and i_q are the dq-axis currents, v_d and v_q are the dq-axis voltages, R_a is the armature winding resistance, L_d and L_q are the armature self-inductances, ω_{re} is the electrical angular velocity of the rotor, ψ_m is the flux linkage of the permanent magnet, and P is the differential operator.

Here, the output torque and the relationship between the electric angular velocity and output torque on the dq-axis are expressed as

$$T_{out} = p\{\psi_m i_q + (L_d - L_q) i_d i_q\}, \quad \text{.....(2)}$$

$$P\omega_{re} = \frac{p}{J}(T_{out} - T_L), \quad \text{.....(3)}$$

where Tout is the output torque, T_L is the load torque, p is the number of pole pairs, and J is the inertia of the motor.

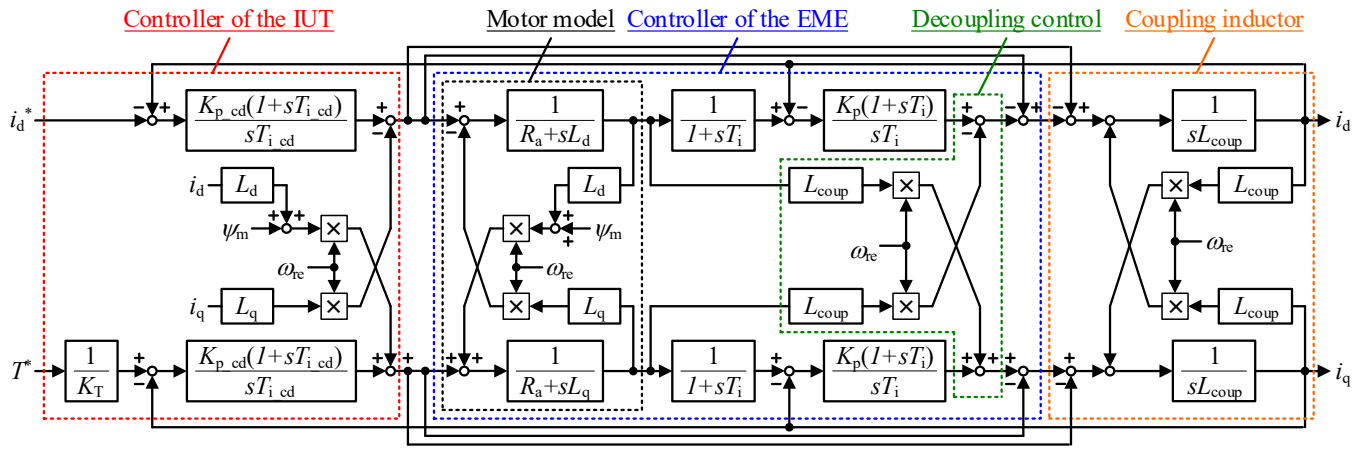

Fig. 2 Block diagram of the inverter test system using a current-source-type EME. The controller detects the IUT output voltage and current. The motor model calculates the motor current from the detected voltage, and the EME current controller reproduces it.

Motor currents are obtained by solving the differential equations (1), (2), and (3) using the backward Euler method in a DSP. Calculated motor currents are sent to the PI current controller as a command. Additionally, feedforward compensation eliminates the interference between the inductors on the dq-axis.

III. Required Current Control Bandwidth

This section analyzes the current control bandwidth required to prevent interference between the current control loops of the IUT and the EME.

Table 1 lists the parameters of the emulated motors. Two motors are used in the analysis to verify the robustness with respect to motor parameter variations.

A. Ideal conditions

Fig. 3 shows the block diagram used for stability analysis, and Table I lists the parameters of the emulated motors. The d-axis current is controlled to zero by the IUT, and feedforward compensation for the cross-coupling terms is applied. This diagram depicts only the q-axis control loop because the d-axis effect is eliminated by feedforward compensation of the cross-coupling terms and by zero d-axis current control. In addition, control and detection delays, parameter mismatches, and output-voltage errors of the power converters are neglected.

Fig. 4 shows the root locus used to determine the stability limit with respect to the EME current control bandwidth for Motor A. Note that the current control bandwidth of the IUT is set to 500 Hz. The poles remain in the left half-plane when the EME current control bandwidth is greater than or equal to 993 Hz. This value corresponds to approximately twice the current control bandwidth of the IUT.

TABLE 1 Emulated motor parameters.

(a)Motor A.

Parameter	Value
Rated power	3.7 kW
Maximum speed	7200 r/min
Maximum torque	4.91 Nm
Number of pole pairs	2
Winding resistance	116 mΩ
d-axis inductance	2.59 mH
q-axis inductance	3.36 mH
Permanent magnet flux	0.0905 Wb
Moment of inertia	30×10^{-4} kgm^2

(b) Motor B.

Parameter	Value
Rated power	5.5 kW
Maximum speed	1500 r/min
Maximum torque	35 Nm
Number of pole pairs	3
Winding resistance	210 mΩ
d-axis inductance	4.3 mH
q-axis inductance	10.2 mH
Permanent magnet flux	0.2001 Wb
Moment of inertia	18×10^{-3} kgm^2

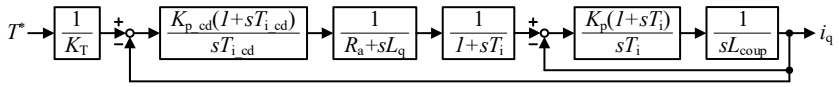

Fig. 3 Analysis model of the relationship between the IUT current control bandwidth and the EME current control bandwidth. This model is used to analyze the stability of the emulator system. The interaction between the current control loops of the IUT and the EME is evaluated to determine the stability limit.

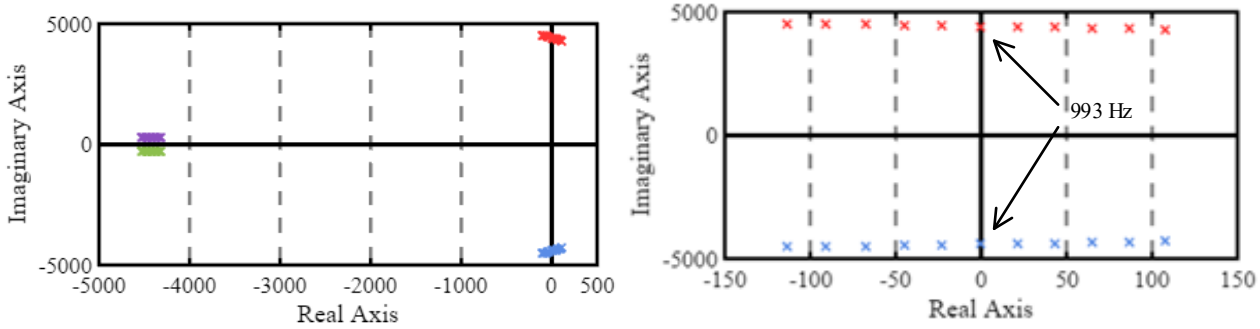

(a) Overview. (b) Focus on the stability limit.

Fig. 4 Root locus for Motor A under the ideal model. The root locus shows the pole locations when the EME current control bandwidth varies.

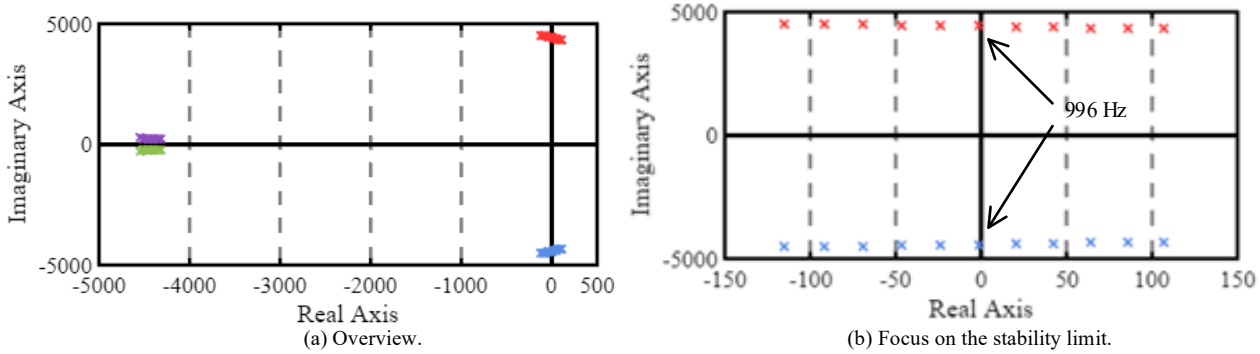

(a) Overview. (b) Focus on the stability limit.

Fig. 5 Root locus for Motor B under the ideal model. The result shows a similar tendency to that of Motor A

Fig. 5 shows the root locus for Motor B under the same conditions as Fig. 4. The overall tendency is almost identical to that of Motor A. The poles remain in the left half-plane when the EME current control bandwidth is greater than or equal to 996 Hz. This value corresponds to approximately twice the current control bandwidth of the IUT.

Fig. 6 shows the required EME current-control bandwidth as the IUT current-control bandwidth varies. The vertical axis represents the ratio of the EME current control bandwidth to the current control bandwidth of the IUT. The required EME current control bandwidth is approximately twice that of the IUT, even when the IUT bandwidth changes. In addition, the required bandwidths for Motor A and Motor B are almost identical, although their output power and rated speed differ. These results indicate that the stability limit is robust against motor parameter variations. Thus, the EME current control bandwidth must be approximately twice the IUT bandwidth to maintain system stability in the ideal model.

B. Including delay conditions

Practical systems include time delays caused by PWM operation, signal detection, sampling, and related processes. These delays significantly affect system stability [13]-[14]. Thus, the required EME current-control bandwidth is analyzed using a model that accounts for the PWM output delay and the current-sensing delay. To simplify the analysis, these delays are modeled as first-order lag systems and inserted into the current control output path and the current feedback path.

Fig. 7 shows the root locus of the stability limit with respect to the EME current control bandwidth for Motor A when practical delays are included in the model. The current control bandwidth of the IUT is set to 500 Hz. The poles remain in the left-half plane when the EME current control bandwidth is greater than or equal to 2386 Hz. This value corresponds to approximately 4.8 times the IUT current control bandwidth. Compared with the ideal model, the required bandwidth increases because the PWM output delay and current sensing delay introduce additional phase lag in the current control loops.

Fig. 8 shows the root locus for Motor B under the same conditions as Fig. 7. The overall tendency is almost identical to that of Motor A despite the different motor parameters. The poles remain in the left-half plane when the EME current control bandwidth is greater than or equal to approximately 2400 Hz, which corresponds to about 4.8 times the IUT current control bandwidth.

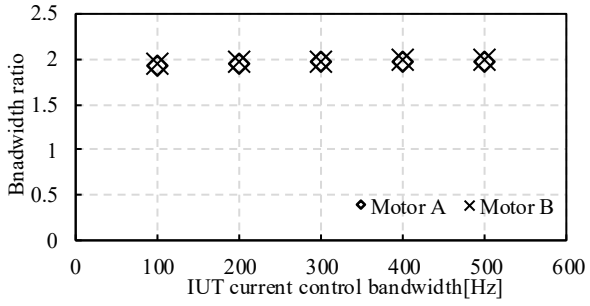

Fig. 6 Stability limit of the ideal model for variations in the IUT current control bandwidth. The vertical axis represents the ratio of the EME current control bandwidth to the IUT bandwidth. The required bandwidth of the EME is approximately twice that of the IUT regardless of the IUT bandwidth.

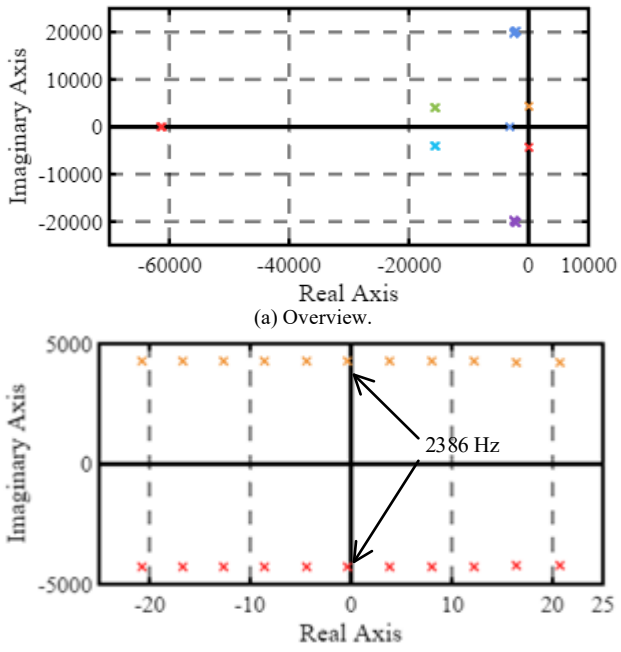

Fig. 7 Root locus for Motor A with the delay-included model. The stability limit increases compared with the ideal model.

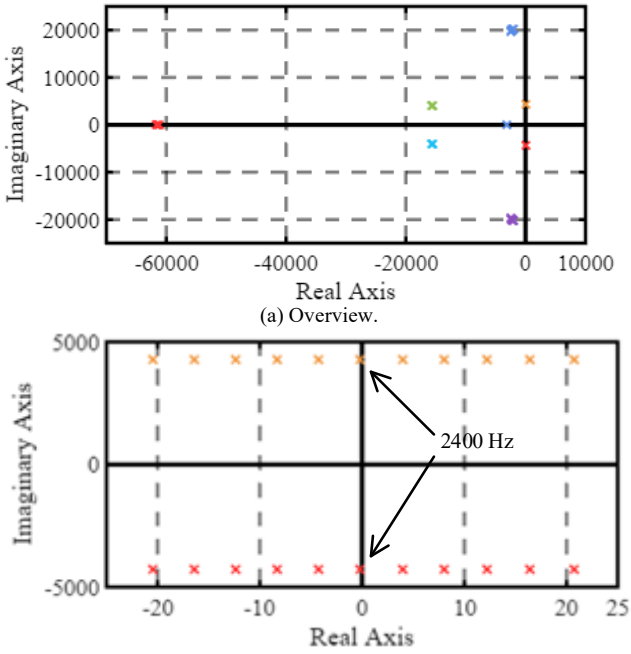

Fig. 8 Root locus for Motor B with the delay-included model. The stability tendency is almost identical to that of Motor A.

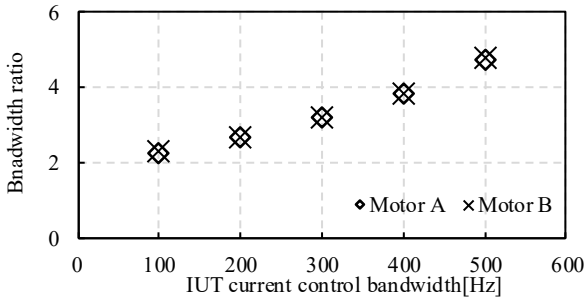

Fig. 9 Stability limit of the delay-included model for variations in the IUT current control bandwidth. The required EME bandwidth increases as the IUT bandwidth increases when delays are included. However, the results for Motor A and Motor B remain almost identical.

Fig. 9 shows the required EME current-control bandwidth when the current-control bandwidth of the IUT varies in the delay-included model. The vertical axis represents the ratio of the EME current-control bandwidth to the IUT current-control bandwidth. Unlike the ideal model shown in Fig. 6, the required bandwidth increases as the IUT current control bandwidth increases because the influence of delay becomes more significant at higher control bandwidths. In contrast, the results for Motor A and Motor B remain almost identical even when the motor parameters differ significantly. These results indicate that the stability condition is robust with respect to motor parameter variations. Thus, under the considered delay conditions, the EME current control bandwidth must be approximately 4.8 times the IUT current control bandwidth to maintain stable operation.

Note that the exact value of the ratio may change when the system delay or control structure is modified, because these factors affect the phase characteristics of the current control loops. Parameters such as the switching frequency, sampling period, and computational delay influence the effective delay in the control system and may therefore alter the stability limit. Nevertheless, these parameters are typically fixed once the control system is designed. Therefore, the significance of this study lies not only in the specific value of 4.8 but also in the analytical approach used to determine the stability limit. By applying the same analysis under the given control and delay conditions, the required EME current-control bandwidth can be systematically determined, providing a practical design guideline for stable current-source-type EMEs.

IV. IUT Output Voltage Detection via LPF

This section analyzes the allowable voltage-detection delay when an LPF is used for detecting the IUT output voltage.

Fig. 10 shows a simplified control block diagram derived from the system shown in Fig. 2. This simplified model is derived under the following assumptions:

(i) The current control response of the EME is faster than that of the IUT, and interference between the two current control loops is neglected.

(ii) The interference between the dq-axis of the IPMSM and the coupling inductor is eliminated by decoupling control of the IPMSM and feedforward compensation of the coupling inductor.

The current control gain of the IUT is designed to achieve a first-order lag response, where the integration time is equal to the electrical time constant of the IPMSM. Although the IUT control is modeled as a first-order lag system to clearly illustrate the effect of the LPF, higher-order current control systems can also be applied. The current control gain of the EME is determined using a second-order standard form, where the coupling inductor is selected as the control target. Consequently, the open-loop transfer function is composed of the integral element of the closed-loop current control of the IUT, the LPF, and the second-order standard form of the closed-loop current control of the EME connected in series.

Fig. 11 shows the open-loop Bode diagram of the simplified model shown in Fig. 10. The gain crossover frequency of the open-loop transfer function corresponds to the LPF cutoff frequency, at which it intersects 0 dB at -20 dB/dec, provided that the LPF cutoff frequency is higher than the current control bandwidth of the IUT. In contrast, the slope

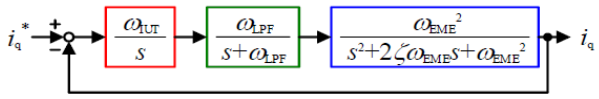

Fig. 10 Simplified control block diagram derived from Fig. 2. This model is used to analyze the influence of voltage detection delay. The LPF is inserted in the voltage detection path.

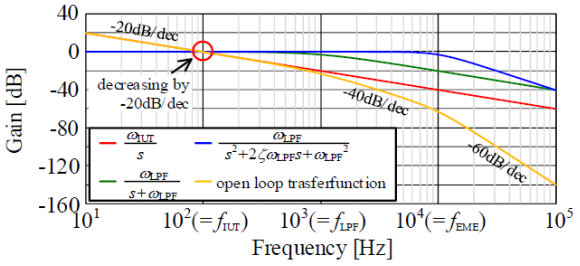

(a) f_{IUT} = 100 Hz, f_{LPF} = 1000 Hz, f_{EME} = 10000 Hz.

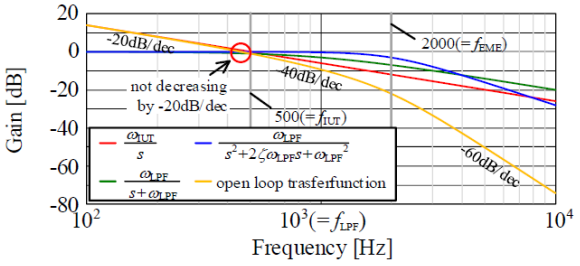

(b) f_{IUT} = 500 Hz, f_{LPF} = 1000 Hz, f_{EME} = 2000 Hz.

Fig. 11 Open-loop Bode diagram of the simplified model shown in Fig. 10. The LPF cutoff frequency determines the gain crossover frequency. The LPF cutoff frequency should be higher than the IUT current control bandwidth.

is steeper than -20 dB/dec and crosses 0 dB at a maximum of -40 dB/dec when the LPF cutoff frequency is close to or below the current control bandwidth of the IUT. Thus, the LPF cutoff frequency should be set higher than the current control bandwidth of the IUT in order to achieve a slower gain gradient near the gain crossover angular frequency in the open-loop Bode diagram.

Fig. 12 shows the closed-loop Bode diagram of the model shown in Fig. 10 for variations in the LPF cutoff frequency. The current control bandwidths of the IUT and the EME are set to 500 Hz and 2000 Hz, respectively. A gain peak occurs when the LPF cutoff frequency is 3 kHz or lower, potentially degrading the current response. In contrast, a gain peak is not observed, and the effect on the current response becomes negligible at an LPF cutoff frequency of 4 kHz. Consequently, the voltage detection delay introduced by the LPF is acceptable when the LPF cutoff frequency is set to at least 8 times the current control bandwidth of the IUT.

From the above, the LPF cutoff frequency must also be high relative to the current control bandwidth of the IUT to prevent a degraded current response. In order to satisfy this condition, the higher the current control bandwidth of the IUT, the higher the cutoff frequency of the LPF must be. However, voltage detection accuracy may deteriorate due to residual harmonic components, thereby preventing accurate calculation of the motor current. Thus, it is necessary to improve the current control response when selecting a low LPF cutoff frequency. This paper employs phase-lead compensation to mitigate the delay introduced by the LPF. The transfer function of phase-lead compensation is expressed as

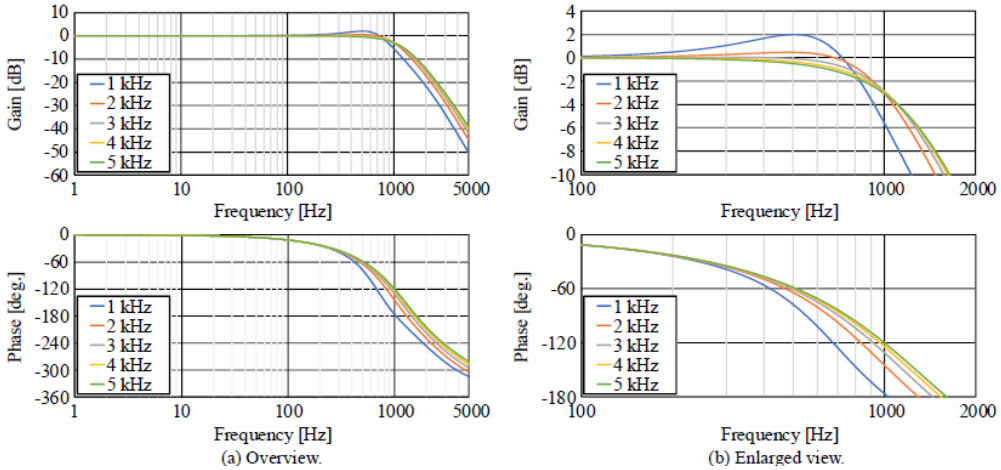

Fig. 12 Closed-loop Bode diagram for variations in the LPF cutoff frequency. The current response deteriorates when the LPF cutoff frequency approaches the IUT current control bandwidth.

$$K(s) = K\frac{T_{\mathrm{comp}}s+1}{\alpha T_{\mathrm{comp}}s+1}, \quad \text{.....(4)}$$

where K is the compensation gain coefficient, T_{comp} is the reciprocal of the break angular frequency, and α is the coefficient that determines the gain compensation range.

The detected voltage via the LPF is compensated by inserting (4) before the motor-model input in the EME controller. A linear approximation of the gain characteristics of the LPF shows that the gain is 0 dB up to the cutoff frequency, after which it decays by -20 dB/dec. Thus, in order to cancel the gain characteristics of the LPF, K should be set to 1, T_{comp} should be set to $1/(2\pi f_{\mathrm{LPF}})$, and α determine the frequency range to be compensated.

V. Experimental Results

This section presents experimental results to verify the analytical results. Table 2 lists the experimental conditions.

Table 2 lists the experimental conditions. The DC bus voltage The DC-link voltage of the EME is set higher than that of the IUT, and the switching frequency of the EME is also set higher than that of the IUT in order to achieve a faster dynamic response.

TABLE 2 Experimental conditions.

Parameter	Value
DC link voltage of IUT	280 V
DC link voltage of EME	320 V
Coupling inductor	1.73 mH
Switching frequency of IUT	10 kHz
Switching frequency of EME	40 kHz

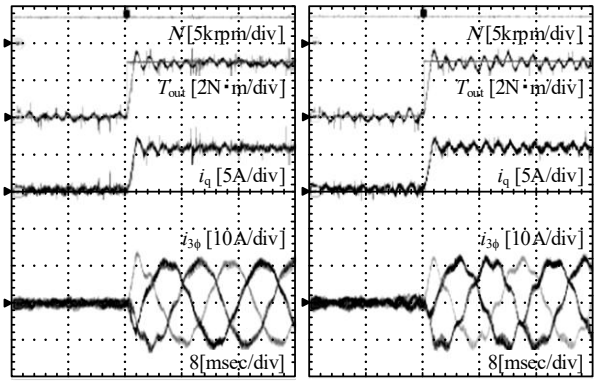

Fig. 13 Torque step response waveforms. The torque response is evaluated under a step torque command. Oscillations appear when the EME bandwidth approaches the stability limit.

A. Required Current Control Bandwidth

Fig. 13 shows the waveforms obtained in response to a 3 Nm torque step command applied to the system. The current control bandwidth of the IUT is set to 500 Hz. In Fig. 13(a), oscillations appear in the torque response but gradually decay. In contrast, in Fig. 13(b), oscillations persist continuously. Moreover, significant distortion appears in the three-phase current waveforms, indicating that the motor current and torque are not properly reproduced. Thus, the stability limit observed in the experiment lies between 2000 Hz and 2050 Hz, which corresponds to approximately four times the IUT current control bandwidth.

According to the analysis in Section III, the stability limit of the EME current control bandwidth is 2386 Hz when the IUT current control bandwidth is 500 Hz. The stability limit obtained from the experiment is lower than the analytical result, with an error of 16.4%. The discrepancy between the analytical and experimental results is mainly attributed to unmodeled damping in the experimental system. In particular, copper loss in the coupling inductor and wiring resistance introduces additional damping that reduces the interaction between the current control loops of the IUT and the EME. Inverter nonidealities, such as dead time and device voltage drops, also reduce the effective loop gain. Although additional delays generally degrade stability, the damping and gain reduction effects are considered to dominate in the experimental system. In practical systems, instability can be avoided by setting the EME current control bandwidth based on the analytical result. Therefore, the simplified analysis provides a useful design guideline for determining the required EME current control bandwidth for stable operation.

B. Allowable PWM voltage detection delay

Fig. 14 shows the difference in current responses with and without an LPF with a 4 kHz cutoff frequency. Note that the voltage command of the IUT is transmitted between the IUT controller and the EME controller to verify inserting the LPF in Fig. 14 (a). Overshoot of the q-axis current is not observed without the LPF. Similarly, overshoot of the q-axis current is

not observed when the LPF with a cutoff frequency of 4 kHz is applied. Thus, setting the LPF cutoff frequency sufficiently higher than the current control bandwidth of the IUT prevents degradation of the current response.

Fig. 15 shows the current responses when the LPF introduces an excessive voltage detection delay. The LPF cutoff frequency is 1 kHz. The parameters of the phase-lead compensator are set to $K = 1$, $T_{comp} = 1/(2\pi f_{LPF})$, and $\alpha = 0.2$. The phase-lead compensator can mitigate the effect of the LPF by selecting a small value of α, although excessively small α makes the compensator close to a pseudo-differentiator. However, (4) becomes a pseudo-derivative form, which may destabilize the EME control. As shown in Fig. 15(a), overshoot appears in the q-axis current, and the phase current becomes distorted with the 1 kHz LPF. In contrast, as shown in Fig. 15(b), applying phase-lead compensation suppresses the overshoot, and no distortion occurs in the phase current. Thus, phase-lead compensation mitigates the excessive voltage detection delay, and the desired current response is maintained even when an LPF with a low cutoff frequency is used.

VI. Conclusion

This paper analyzed the allowable voltage-detection delay and the required current-control bandwidth for a DSP-based current-source-type EME. First, the minimum current-control bandwidth required to prevent interference between the IUT and EME current-control loops was clarified. The required EME current-control bandwidth is analyzed under practical conditions where PWM output delay and current-sensing delay are approximated as first-order lag systems. The analytical results indicate that the required EME current-control bandwidth is approximately 4.8 times that of the IUT, which has a current-control bandwidth of 500 Hz.

Second, the allowable voltage-detection delay when using an LPF was investigated. The analysis showed that the LPF cutoff frequency should be at least 8 times higher than the IUT current control bandwidth to avoid degrading the current response. In addition, phase-lead compensation was applied to mitigate the influence of the detection delay.

Experimental results validated the analytical results. The stability limit obtained from the experiment was approximately four times the IUT current control bandwidth, which was close to the analytical prediction. These results demonstrate that stable motor emulation can be achieved without relying on high-performance voltage detection hardware. Therefore, the proposed design guidelines facilitate the practical implementation of DSP-based current-source-type EMEs, particularly for large-capacity motor-drive applications.

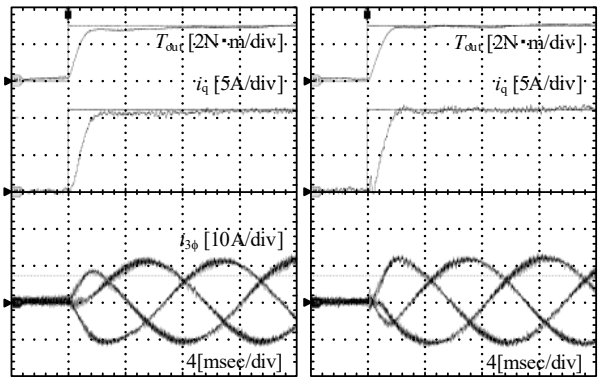

(a) W/O LPF. (b) W/ LPF (f_{LPF} = 4 kHz).

Fig. 14 Current response with an acceptable LPF cutoff frequency. The current response does not deteriorate when the LPF cutoff frequency is sufficiently higher than the IUT bandwidth.

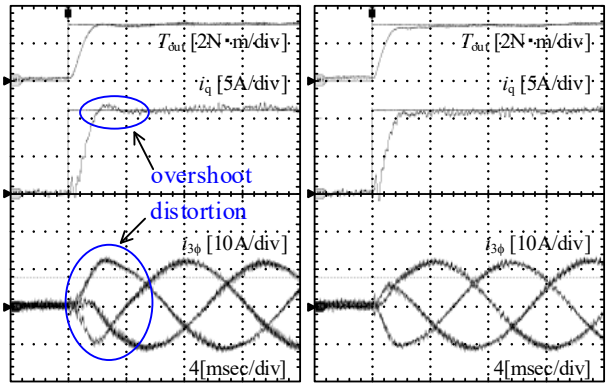

(a) W/O compensation. (b) W/ compensation.

Fig. 15 Current response with LPFs introducing excessive voltage detection delay with and without compensation. The effect of the LPF has been removed from the current response via phase-lead compensation.

Acknowlendgments

This work was supported by JST SPRING, Japan Grant Number JPMJSP2189.

References

[1] Kazuki Nakamura, Kaya Kawashima, Ryoko Kato, Kohsuke Seki, Kenta Yamabe, Kantaro Yoshimoto, and Tomoki Yokoyama, "Verification of 1 MHz Multisampling Disturbance Compensation Deadbeat Control for Megawatt-Level Grid-Tied Multi-level Inverter using Hardware-in-the-loop Controller", IEEJ Journal of Industry Applications, Volume 12, Issue 3, pp. 427--433, 2023.

[2] Takashi Yamada, Kazuki Semba, Hiroyuki Sano, and Yusaku Suzuki, "Simulation Based Design, a Necessity for Advanced Design and Requirement for CAE Tools", IEEJ Journal of Industry Applications, Volume 12, Issue 1, pp. 1-11, 2023.

[3] K. Etzold et al., "Function Development With an Electric-Machine-in-the-Loop Setup: A Case Study," in IEEE Transactions on Transportation Electrification, vol. 5, no. 4, pp. 1419-1429, Dec. 2019.

[4] A. S. Abdelrahman, K. S. Algarny and M. Z. Youssef, "A Novel Platform for Powertrain Modeling of Electric Cars With Experimental Validation Using Real-Time Hardware in the Loop (HIL): A Case Study of GM Second Generation Chevrolet Volt," in IEEE Transactions on Power Electronics, vol. 33, no. 11, pp. 9762-9771, Nov. 2018.

[5] Q. Li, D. Wang, J. Lin, F. Jian, Z. Wang, and C. Ma, "Improving Dynamic Accuracy of the Electric Motor Emulator at High Speed via MIMO Design Method," in IEEE Transactions on Power Electronics, vol. 37, no. 12, pp. 14395-14407, Dec. 2022.

[6] Chia-Chou Chang, Che-An Cheng, and Yaow-Ming Chen, "Modeling and Analysis of Model-Based Feedforward Voltage Terms for Closed-loop Current Control in PMSM Electric Motor Emulators", IEEJ Journal of Industry Applications, Volume 13, Issue 5, pp. 570--577, 2024.

[7] Y. Qi, K. Ma, and W. Tang, "Full-Bandwidth Mission Profile Emulation of the Electric Machine System With Voltage Reference Signal Transmission," in IEEE Transactions on Power Electronics, vol. 37, no. 3, pp. 3473-3483, March 2022.

[8] Y. Luo, M. A. Awal, W. Yu, and I. Husain, "FPGA-Based High-Bandwidth Motor Emulator for Interior Permanent Magnet Machine Utilizing SiC Power Converter," in IEEE Journal of Emerging and Selected Topics in Power Electronics, vol. 9, no. 4, pp. 4340-4353, Aug. 2021.

[9] K. S. Amitkumar, P. Pillay and J. Bélanger, "An Investigation of Power-Hardware-in-the-Loop- Based Electric Machine Emulation for Driving Inverter Open-Circuit Faults," in IEEE Transactions on Transportation Electrification, vol. 7, no. 1, pp. 170-182, March 2021.

[10] Y. -R. Lee, Y. -C. Kwon and S. -K. Sul, "DC-Link Voltage Design of High-Bandwidth Motor Emulator for Interior Permanent-Magnet Synchronous Motors," 2018 IEEE Energy Conversion Congress and Exposition (ECCE), Portland, OR, USA, 2018, pp. 4453-4459.

[11] K. S. Amitkumar, R. Sudharshan Kaarhik, and Pragasen Pillay, "A Versatile Power-Hardware-in-the-Loop-Based Emulator for Rapid Testing of Transportation Electric Drives," in IEEE Transactions on Transportation Electrification, vol. 4, no. 4, December 2018.

[12] Lei Zhu, Dong Jiang, Ronghai Qu, Leon M. Tolbert, and Qiao Li, "Design of Power Hardware-in-the-Loop Simulations for Integrated Starter-Generator Systems," in IEEE Transactions on Transportation Electrification, vol. 5, no. 1, March 2019.

[13] Yuanhao Xie, Dong Jiang, and Zicheng Liu, "Improved Accuracy of Power Electronic-Based Motor Emulation With Compensation for Signal Transmission Delay", in IEEE Transactions on Transportation Electrification, Vol. 8, no. 1, March 2022.

[14] Hiroki Takahashi and Jun-ichi Itoh, “Control Method for a Matrix Converter to Ensure Compatibility between Filter Resonance Suppression and Output Current Control Performance”, in IEEJ Transaction on Industry Applications, Vol. 135, No. 7, pp. 802-815, 2015.